OPEN ACCESS



Deep Synoptic Array Science: A Massive Elliptical Host Among Two Galaxy-cluster Fast Radio Bursts

Kritti Sharma¹, Jean Somalwar¹, Casey Law^{1,2}, Vikram Ravi^{1,2}, Morgan Catha², Ge Chen¹, Liam Connor¹, Jakob T. Faber¹, Gregg Hallinan^{1,2}, Charlie Harnach², Greg Hellbourg^{1,2}, Rick Hobbs², David Hodge¹, Mark Hodges², James W. Lamb², Paul Rasmussen², Myles B. Sherman¹, Jun Shi¹, Dana Simard¹, Reynier Squillace¹, Sander Weinreb¹, David P. Woody², and Nitika Yadlapalli¹

Abstract

The stellar population environments that are associated with fast radio burst (FRB) sources provide important insights for developing their progenitor theories. We expand the diversity of known FRB host environments by reporting two FRBs in massive galaxy clusters that were discovered by the Deep Synoptic Array (DSA-110) during its commissioning observations. FRB 20220914A has been localized to a star-forming, late-type galaxy at a redshift of 0.1139 with multiple starbursts at lookback times less than ~3.5 Gyr in the A2310 galaxy cluster. Although the host galaxy of FRB 20220914A is similar to typical FRB hosts, the FRB 20220509G host stands out as a quiescent, early-type galaxy at a redshift of 0.0894 in the A2311 galaxy cluster. The discovery of FRBs in both late- and early-type galaxies adds to the body of evidence that the FRB sources have multiple formation channels. Therefore, even though FRB hosts are typically star-forming, there must exist formation channels that are consistent with old stellar population in galaxies. The varied star formation histories of the two FRB hosts that we report here indicate a wide delay-time distribution of FRB progenitors. Future work in constraining the FRB delay-time distribution, using the methods that we develop herein, will prove crucial in determining the evolutionary histories of FRB sources.

Unified Astronomy Thesaurus concepts: Radio transient sources (2008); Galaxy clusters (584); Elliptical galaxies (456); Star formation (1569)

1. Introduction

Characterizing the stellar population in the neighborhood of extragalactic transients can unveil the nature of their progenitors. The morphology, color, metallicity, age, and star formation history of the host galaxies of supernovae have helped to constrain their numerous explosion channels (Svensson et al. 2010; Pan et al. 2014; Hakobyan et al. 2020; Irani et al. 2022). The hunt for correlations with the host galaxy's stellar mass and metallicity (Kelly et al. 2014), studies of nucleus-offset distribution (Bloom et al. 2002), and ongoing recent star formation (Blanchard & Berger 2016) have revealed that the progenitors of long gamma-ray bursts have a short lifetime, prefer dense and low-metallicity stellar environments, and are likely to be found in young starbursts of blue star-forming galaxies with high specific star formation rates (Levesque et al. 2010; Perley et al. 2016). Similar studies for short gamma-ray bursts have revealed that the hosts are more luminous and are found in less actively starforming regions than long gamma-ray bursts (Berger 2009). The large nucleus-offsets suggested that short gamma-ray burst progenitors migrate from stellar nurseries to explosion sites, thus hinting toward kicks during the merger of compact object binaries (Fong & Berger 2013; Fong et al. 2022).

The studies of fast radio burst (FRB) host galaxies, enabled by arcsecond-scale localization by modern radio interferometers,

Original content from this work may be used under the terms of the Creative Commons Attribution 4.0 licence. Any further distribution of this work must maintain attribution to the author(s) and the title of the work, journal citation and DOI.

have attempted to solve the long-standing mystery of these energetic, short-duration enigmatic explosions (Heintz et al. 2020; Mannings et al. 2021; Bhandari et al. 2022; Gordon et al. 2023). The major conclusions from such studies have been actively incorporated into proposed progenitor models (Petroff et al. 2019, 2022). For example, the association of FRB 20121102 with a dwarf, rapidly star-forming galaxy and a persistent radio source suggested a young magnetar progenitor (Kulkarni et al. 2015; Chatterjee et al. 2017; Tendulkar et al. 2017). However, the discovery of a repeating FRB 20200120E associated with a globular cluster of M81 indicated that the progenitor was formed in a compact binary coalescence event (Bhardwaj et al. 2021; Kirsten et al. 2022). Diagnostics such as inferred local environments, galaxy types, and accurately derived physical properties of a large sample of host associations can help to disentangle the proposed progenitor theories and differentiate FRBs from other extragalactic transients (Petroff et al. 2022). These studies can determine if FRBs are formed via one or multiple progenitor channels because FRBs have been found in a spectrum of environments, including dwarf galaxies (Bassa et al. 2017; Bhandari et al. 2023), spiral galaxies (Marcote et al. 2020; Fong et al. 2021; Mannings et al. 2021; Tendulkar et al. 2021), and globular cluster (Bhardwaj et al. 2021; Kirsten et al. 2022). The existing sample of host galaxies of FRBs suggests that they are generally star-forming (Gordon et al. 2023). The distribution of stellar properties of FRB hosts has been found to be inconsistent with that of long gamma-ray bursts and superluminous supernovae, with a probable analogy with magnetars

Cahill Center for Astronomy and Astrophysics, MC 249-17 California Institute of Technology, Pasadena CA 91125, USA; kritti@caltech.edu

Owens Valley Radio Observatory, California Institute of Technology, Big Pine CA 93513, USA

Received 2023 February 28; revised 2023 April 7; accepted 2023 April 18; published 2023 June 23

formed in core-collapse supernovae (Bochenek et al. 2021; Piro et al. 2021).

Motivated by these studies, in this article we present a detailed analysis of two new FRBs, FRB 20220914A and FRB 20220509G, both of which are located within massive galaxy clusters (Connor et al. 2023). While the host galaxy of FRB 20220914A is a star-forming galaxy with a bursty star formation history, the host galaxy of FRB 20220509G is the first early-type quiescent FRB host. In Section 2, we discuss Deep Synoptic Array (DSA-110)³ detection of these two FRBs and the optical data obtained for their host galaxies. We present our analysis framework and derived galaxy properties in Section 3. Meanwhile, in Section 4, we compare our FRBs with the existing sample of localized FRBs, the galaxy population, and other extragalactic transients, along with the first attempt to formulate, model, and constrain their delay-time distribution. We discuss the implications of our results and summarize this article in Section 5. Throughout, we adopt the Planck13 cosmology (Planck Collaboration et al. 2014), where Hubble constant $H_0 = 67.8 \,\mathrm{km \, s^{-1}} \,\mathrm{Mpc^{-1}}$, cosmological constant $\Omega_{\Lambda} = 0.69$, and matter-density parameter $\Omega_{\rm m} = 0.31$.

2. Observations

In this section, we focus on the optical follow-up observations of the host galaxies of FRB 20220509G and FRB 20220914A. A description of the DSA-110 discovery and radio properties of these FRBs is presented in a companion article (Connor et al. 2023). FRB 20220509G was localized to (R.A. J2000, decl. J2000) = $18^{h}50^{m}40^{s}8$, $+70^{d}14^{m}37.8$, with a 90% error ellipse with axes 4".7 and 3".2 in R.A. and decl. respectively. FRB 20220914A was localized to (R.A. J2000, J2000) = $18^{h}48^{m}13^{s}.63$, $+73^{d}20^{m}12^{s}.89$, with a 90% error ellipse with axes 2"0 and 1"6 in R.A. and decl. respectively. The localization procedures were identical to those described in Ravi et al. (2023). With regards to the radio properties, it is particularly noteworthy that while no polarized signal or scattering was detected from FRB 20220914A, FRB 20220509G shows evidence for temporal broadening due to scattering with a timescale of $80\pm20\,\mu s$ at $1498.75\,\mathrm{MHz}$, and a Faraday rotation measure of $-111.54\pm1.50\,\mathrm{rad\,m^{-2}}$ in the observer frame (Sherman et al. 2023, in preparation). The extragalactic DMs of both FRBs are likely to be dominated by the intracluster medium of the host galaxy clusters (Connor et al. 2023).

The PanSTARRS1 (PS1; Chambers et al. 2016) *i*-band images of galaxies that are coincident with the 90% confidence localization region of these FRBs are displayed in Figure 1. We use astropath to calculate the association probability for each FRB to nearby galaxies (Aggarwal et al. 2021). The fields of both FRBs have been observed as part of the DESI Legacy Surveys in g, r, and z bands. The 5σ point-source depth of the Legacy Surveys is r=23.9 (DR6; MzLS+BASS region; Dey et al. 2019). The sensitivity to typical galaxies is about 0.2 MAG shallower. For each FRB, we build a galaxy catalog by selecting resolved sources within 30'' of the FRB with the astro-datalab Python library. The star in the foreground of FRB 20220509G is identified and removed as a point source in our cross-match analysis. To calculate an association probability, astropath requires the FRB position and error, as well as each galaxies

position, magnitude (we use r-band), and half-light radius. We use the adopted priors that were recommended in Aggarwal et al. (2021), which assumes an exponential FRB angular offset distribution and an association probability that scales inversely to the number density of galaxies at a given magnitude ("exp" and "inverse," respectively). We further assume a prior on an undetected host in flux-limited data, P(U) = 0.1, which provides reliable and accurate estimates in realistic FRB host simulations (Seebeck et al. 2021). Following this procedure, we find that FRB 20220509G is associated to a host galaxy at $(R.A. J2000, decl. J2000) = 18^h 50^m 41^s 92, +70^d 14^m 33^s 95$ with 1% false association probability. This galaxy is cataloged as 2MASX J18504127+7014359 (J1850+70 hereafter) in the NASA Extragalactic Database (Helou et al. 1991). We note that no other galaxy in the field of FRB 20220509G has an association probability greater than 10^{-7} . FRB 20220914A is associated to a host galaxy at (R.A. J2000, decl. $J2000) = 18^{h}48^{m}13^{s}96, +73^{d}20^{m}10^{s}70$ (J1848+73 hereafter) with 3% false association probability. The second most likely association has an r-band magnitude of 22.7 with an association probability of 2% and is northwest of the most likely host. We note that for both the FRBs, with P(U) = 0.1, no other galaxies in the field have a significant association probability.

We obtained the optical spectrum of both the host galaxies with the Low-Resolution Imaging Spectrometer on the Keck I telescope (Keck I/LRIS Oke et al. 1995). However, we could only use the blue component of the detector due to instrument malfunction during the night of observations, so a mirror was used to direct light only into the blue arm. The light was dispersed using a 300/5000 grism. Single exposures of 1800 and 500 s were obtained on 2022 October 18 using a 1" slit at a position angle of 236°.40 and 299°.95 in good observing conditions with seeing of 0."84 and 0."95 for J1848+73 and J1850+70 respectively. The slit positions that were used to extract the galaxy spectra are indicated in Figure 1. The restframe line FWHM was approximately 9.5 Å. The spectra were reduced with the standard lpipe software (Perley 2019) and calibrated using observations of the standard star BD+28 4211. We further scale the spectrum to match PS1 g-band photometry (described in Section 3.1) to account for slit losses.

The spectrum of J1848+73 exhibits strong emission lines and absorption features, thus indicating a composition of young and old stellar populations in this galaxy (Figure 1). We measure the spectroscopic redshift of the host galaxies using the Penalized PiXel-Fitting software (pPXF; Cappellari 2017, 2022) by jointly fitting the stellar continuum and nebular emission using the MILES stellar library (Sánchez-Blázquez et al. 2006). The best pPXF fit to the spectrum has a reduced- χ^2 of 0.9076 (number of degrees of freedom, $N \sim 1000$) and reveals a redshift of 0.1139 ± 0.0001 . The Milky Way galactic dust extinction corrected measured line flux of [O II] and $H\beta$ lines are $(2.90 \pm 0.10) \times 10^{-16} \text{erg s}^{-1} \text{cm}^{-2}$ and $(1.16 \pm 0.03) \times$ 10⁻¹⁷erg s⁻¹cm⁻², respectively. The star formation rate (SFR) using the [O II] luminosity and calibrated using the Kennicutt (1998) calibration is measured to be $0.14 \pm 0.10 \, M_{\odot} \, \mathrm{yr}^{-1}$. We note that these SFR measurements are not corrected for the dust extinction within the host galaxy, and hence these SFRs serve as a lower limit on the true SFR.

The strong [Ca II], H β and [Mg II] absorption features with [O II] emission are evident in the spectrum of J1850+70, thus indicating that it is an early-type galaxy (Figure 1). The

³ https://deepsynoptic.org

⁴ https://github.com/astro-datalab/datalab/

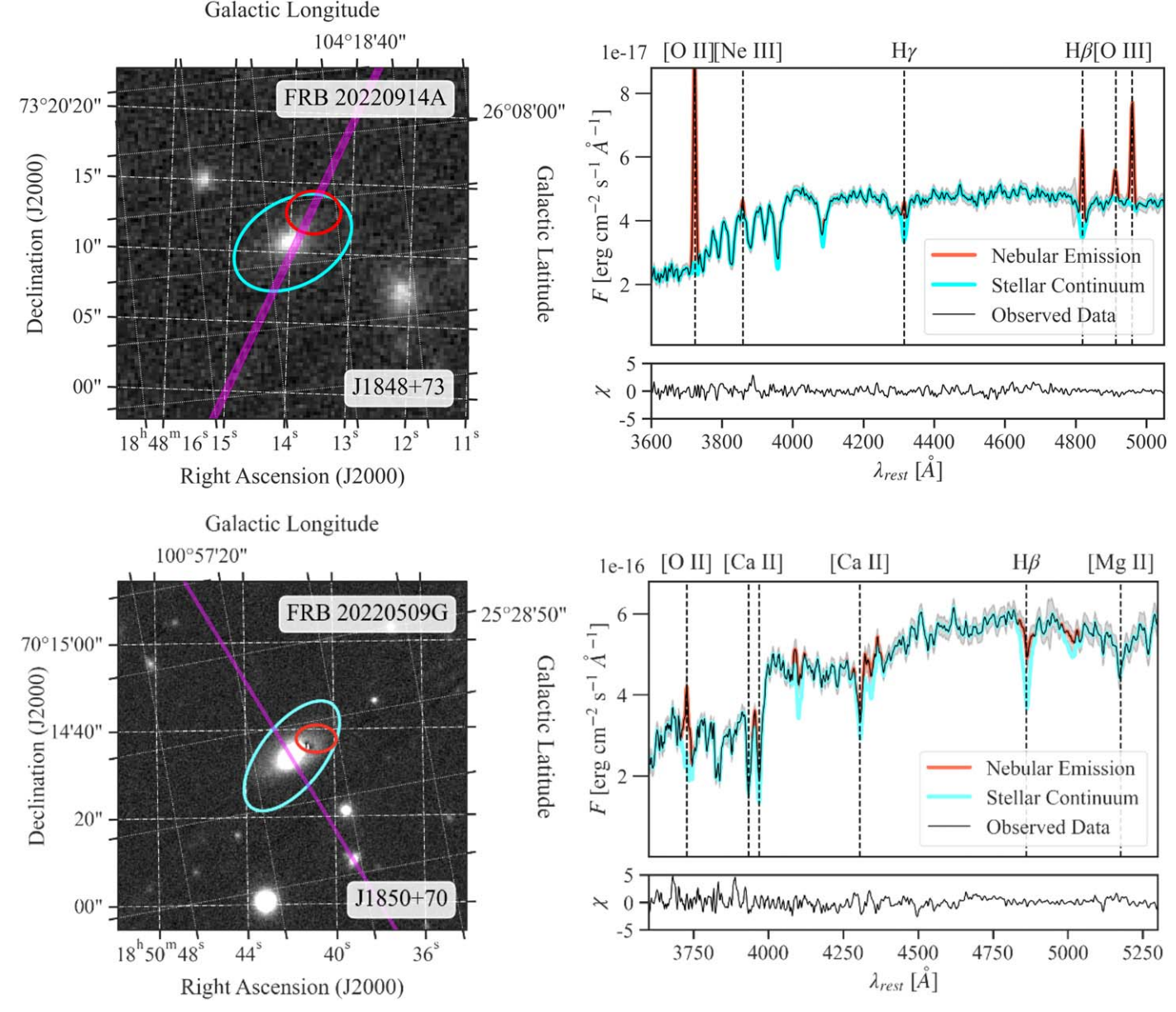


Figure 1. Optical data for the host galaxies of FRB 20220914A (top row) and FRB 20220509G (bottom row). The flux-conservative isophote for photometry (cyan), the slit positions for spectroscopy with Keck I/LRIS (magenta) and 90% confidence localization region (red) of both the FRBs overplotted on the PS-1 *i*-band images are displayed in the left-hand panels. The pPXF fits to the stellar continuum (cyan) and nebular emission (red) with corresponding residuals in our Keck I/LRIS optical spectra (black) of both the host galaxies are included in the right-hand panels.

spectroscopic redshift of J1850+70 is also measured using pPXF, where the best fit with a reduced- χ^2 of 1.0166 (N \sim 1000) indicates a redshift of 0.0894 \pm 0.0001. The Milky Way galactic dust extinction corrected [O II] line flux is $(8.74 \pm 1.39) \times 10^{-17} {\rm erg \ s^{-1} cm^{-2}}$, which corresponds to an SFR of $0.04 \pm 0.01 \ M_{\odot} \ {\rm yr^{-1}}$. An upper limit on the H β line emission is $(2.18 \pm 1.04) \times 10^{-17} {\rm erg \ s^{-1} cm^{-2}}$. This corresponds to an [O II]/H $\beta \gtrsim 2.71$ at 1σ level, which is greater than the expected typical value for field galaxies (Kewley et al. 2004), thus indicating low star formation in this galaxy.

3. Analysis Framework

In this section, we describe the analysis framework that was used to derive the properties of host galaxies using their photometric and spectroscopic data.

3.1. Isophotal Analysis

We executed photometry on archival images of PS1, Two Micron All Sky Survey (2MASS; Skrutskie et al. 2006) and ALLWISE (Cutri et al. 2021) surveys. The 5σ limiting magnitude of 2MASS data for the J1848+73 galaxy are J=19.7 mag, H=18.8 mag and $K_s=18.1$ mag. Due to shallow depth, this galaxy is marginally detected in 2MASS data, and hence, we do not include these data in our analysis. Furthermore, this galaxy is not detected in ALLWISE data. We iteratively fit elliptical isophotes to the PS1 i-band image of the galaxy using standard procedures defined in photutils (Bradley et al. 2022) to identify the isophote that captures $\gtrsim 95\%$ of the light from the galaxy. The best isophote indicated by our isophotal analysis has a semimajor axis of 4.0000 with an ellipticity of 0.326 (Figure 1). We convolve this aperture with the point-spread function of all images to measure the instrumental magnitudes in all bands. This

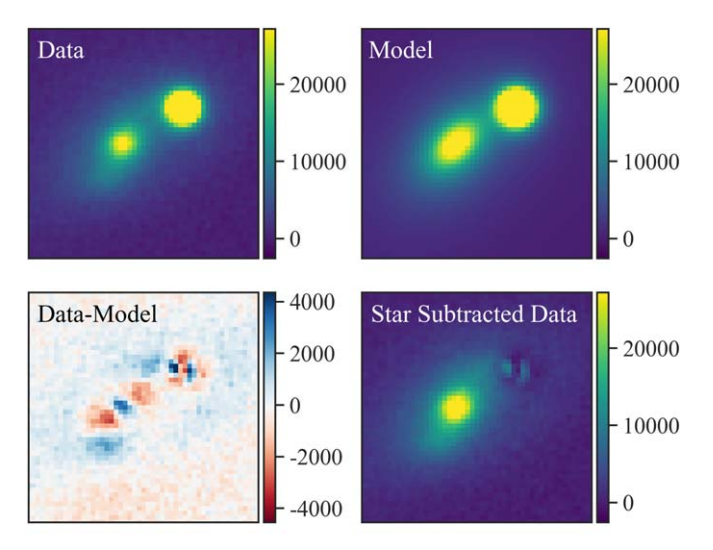


Figure 2. The host galaxy of FRB 20220509G has a bright star present at an angular separation of 4'', as can be seen in the *i*-band image of this galaxy in the top left-hand panel. We model the star and the galaxy with circular and elliptical moffat profiles, respectively (top right-hand panel), and test the quality of subtraction by subtracting this model from the data (bottom left-hand panel). The total counts in a 5'' aperture at the star's location are consistent with zero, thus confirming an acceptable subtraction quality. The final star-subtracted data is displayed in the bottom right-hand panel.

instrumental magnitude is then corrected using zero-point, interstellar dust reddening, and extinction to obtain the AB magnitudes (Fitzpatrick 1999; Green 2018).

The data for the J1850+70 galaxy are contaminated by the presence of a bright star at an angular separation of $\sim 4''$. The typical method for photometry involves either masking the pixels at the location of the star or, equivalently, using a smaller aperture focused at the center of the galaxy. However, we note that our galaxy is extended, and masking out those pixels will reduce its flux, and hence its stellar mass estimate. We confirm this by redoing our SED analysis (described in the following section), while using a smaller aperture size capturing the nuclear region of $\sim 2''$ radius. We note that while the recent SFR remains consistent with zero, the stellar mass ($\log M_*$) drops by \sim 5%. Therefore, in order to perform photometry, we fit a circular moffat profile to the star and subtract it from our data. The quality of subtraction is assessed by jointly fitting an elliptical moffat profile to the galaxy and a circular moffat profile to the star, and ensuring approximately zero counts in a 5" aperture around the star (Figure 2). We note that we also tried fitting an elliptical moffat profile to the star, which resulted in a similar subtraction quality. Hence, we choose to use a circular moffat profile for the star. In this fitting procedure, all of the parameters of the circular and elliptical moffat profiles, including their centered x and y coordinates and amplitude, are jointly fitted. In Figure 2, the counts in a 5" aperture at the star's location in the star-subtracted data are 99.81 counts pixel⁻¹, which is comparable to the 98 counts pixel-1 of background. The ratio of the stars flux in the data to the rms of counts in star-subtracted data is \geq 3000. The pixel scale of 2MASS data is 1" pixel⁻¹ with a typical FWHM of 2"5 in all bands. Due to the compact point-spread function of the star and very low counts of the galaxy, the star subtraction is poor in H and K_s bands. Hence, we do not include these two bands in our analysis. Furthermore, the signal-to-noise ratio of the galaxy detection is poor in

ALLWISE W3 and W4 bands, and hence they are not included in our analysis.

The isophotal analysis of the star-subtracted i-band image of the galaxy reveals an elliptical flux-conservative profile (i.e., the one that captures $\gtrsim 95\%$ of the flux from the galaxy) with a semimajor axis of $15.^{\prime\prime}.48$ and an ellipticity of 0.52 (Figure 1). The axial ratio of its half-light isophote is 0.59. At low redshifts, the probability distribution of the axial ratio for spirals is flat, whereas it rises for elliptical galaxies, thus indicating that it is potentially an elliptical galaxy (Rodríguez & Padilla 2013). However, an axial ratio of 0.59 also implies a significant bulge dominance, which is typical of lenticular galaxies, and hence this possibility cannot be ruled out based on the ellipticity measurements alone. In Section 3.2, we present more evidence to resolve the host galaxy classification for FRB 20220509G.

3.2. SED Analysis

We use the stellar population synthesis modeling software Prospector (Johnson et al. 2021), which uses the Flexible Stellar Population Synthesis (FSPS; Conroy et al. 2009; Conroy & Gunn 2010), to determine the stellar properties of our host galaxies. We simultaneously model and fit for the observed photometry and spectroscopy. Due to underestimated photometric errors and imperfect subtraction of the star, we assume additional 10% photometric errors for both galaxies. Typically, 5% photometric errors are assumed in the recommended procedures by Prospector developers (Johnson et al. 2021). Given that the star subtraction is imperfect, we tested the robustness of our measurements to changes in assumed photometric errors by varying it to 5%, 10%, and 20%. On this increase in photometric errors, while the SFR of the galaxies remained the same within the error bars, the stellar mass of the galaxies was reduced by \lesssim 5%. Since the impact of this change on the final conclusions of our analysis is insignificant, we make a conservative choice of 10% photometric errors for both galaxies.

We initialize the redshift to the value obtained from pPXF fits with a uniform prior width of 1%. We chose to use a continuity non-parametric star formation history with seven bins to avoid systematics induced by parametric star formation histories (Conroy 2013; Leja et al. 2017). As recommended in Johnson et al. (2021), we use the StudentT prior on the SFR ratios in adjacent bins. This prior is similar to a Gaussian prior with more probability in the tails and ensures that the returned SFH is a constant SFR in the absence of any constraint from the data.

We assume the Kroupa (2001) initial mass function. We include nebular continuum and line emission in our model, which is based on the CLOUDY implementation within FSPS (Ferland et al. 2013). We tie the nebular emission metallicity to the stellar metallicity and float the nebular ionization parameter. The nebular emission model assumes that all of the nebular emission is produced by the young stellar population, which may not always be true in galaxies where they are instead powered by active galactic nuclei or shocks (Yan et al. 2006). To account for such cases, we marginalize the amplitude of emission lines in our observed spectrum. We include dust emission in the model but fix all of the dust emission parameters due to lack of good quality data at infrared wavelengths (Draine & Li 2007). We use spectral smoothing and a 12th-order Chebyshev polynomial for

Table 1
Summary of Free and Fixed Parameters Used in Our Spectral Energy
Distribution (SED) Analysis

Parameter	Value	Prior
SFH		
$\log M_* [M_{\odot}]$	10	Uniform(8, 12)
$r_i^{\mathbf{a}}$	0	StudentT(0, 0.3, 2)
$\log z/z_{\odot}$	-0.2	Uniform(-2.0, 0.2)
$N_{\rm bins}^{}$	7	•••
Zred	z' ^c	Uniform(z' -0.01, z' +0.01)
Dust Attenuation		
τ _{5500, diffuse} d	0.5	$\mathcal{N}(0.3, 1.0, 0, 4)$
Nebular Emission		
$U_{\mathrm{neb}}^{\mathbf{e}}$	-2	Uniform(-4, -1)
$W_{\text{eline}}^{\text{f}}$	1	Uniform(0.01, 100)
$\sigma_{ m eline}^{{ m g}}$	200	Uniform(30, 500)
Dust Emission ^h		
$U_{ m min,\ dust}$	1	•••
Q_{PAH}	4	
$\gamma_{ m dust}$	0.001	•••
Spectral Calibration		
$\sigma_{ m smooth}^{}$	200	Uniform(30, 500)

Notes.

- ^a Ratio of SFR in *i*th and its adjacent bin.
- ^b Number of bins in the non-parametric star formation history.
- ^c Best-fit redshift from pPXF.
- ^d Opacity at 5500 Å describing the attenuation of old stellar light.
- ^e Nebular ionization parameter.
- f Width of emission line amplitude prior (Johnson et al. 2021).
- ^g Emission lines broadening parameter.
- ^h Parameters from Draine & Li (2007) emission model.
- i Spectral resolution.

parameterized spectrophotometric calibration. The set of parameters in our model and corresponding priors are summarized in Table 1. We sample from the posterior using the ensemble sampler emcee (Foreman-Mackey et al. 2013). For a discussion on best practices in SED modeling, we refer the reader to the appendix and the references therein.

The SED fits for the host galaxies of FRB 20220914A and FRB 20220509G are displayed in Figures 3 and 4, respectively, and the corresponding observed and derived parameters are summarized in Table 2. We observe that all of the nebular emission and absorption features, along with the photometry, are well fitted by the model with a reduced- χ^2 of 1.014 and 1.477 ($N \sim 1000$) for the two galaxies. The star formation history of the host galaxy of FRB 20220914A indicates a variety of stellar population ages, which is consistent with our inference from the spectrum (as discussed in Section 2). The high dust attenuation, $A_V = 1.64^{+0.22}_{-0.23}$ and stellar mass, $\log M_*(M_\odot) = 9.99^{+0.09}_{-0.09}$ with significant ongoing star formation averaged over the last 100 Myr, $SFR = 1.45^{+1.05}_{-0.61} M_{\odot} \text{yr}^{-1}$ indicates that it is a star-forming spiral galaxy. Meanwhile, the star formation history of FRB 20220509G indicates a very old stellar population, which is also consistent with it being an early-type galaxy (as discussed in Section 2). The low dust attenuation $A_V = 0.19^{+0.04}_{-0.04}$ supports our argument of it being an elliptical galaxy (as discussed in Section 3.1). Furthermore, a high stellar mass, $\log M_*(M_\odot) = 11.13^{+0.02}_{-0.02}$ and a consistent

with zero SFR averaged over the last $100\,\mathrm{Myr}$, $\mathrm{SF}R = 0.08^{+0.06}_{-0.04}\,M_\odot$ yr⁻¹ implies that this is a quiescent galaxy. We note that SFR measured using [O II] emission line luminosity in Section 2 is a lower limit on the actual SFR because they are not corrected for dust attenuation within the host galaxy itself. The SFRs measured from our SED analysis are corrected for the dust attenuation within the host galaxies, and hence are consistent with the lower limits on SFRs (as reported in Section 2).

4. Nature of FRB Progenitors

In this section, we compare the host galaxies of FRB 20220509G and FRB 20220914A with the hosts of other FRBs, the background galaxy population, and the hosts of other transient populations. Along with our two FRBs, we include the sample of 23 FRB hosts published in Gordon et al. (2023), which includes refined host properties computed with non-parametric SED modeling for FRBs published in Heintz et al. (2020), Bhandari et al. (2023), Bhandari et al. (2022), and Mannings et al. (2021). We also include the previously reported non-repeating FRBs discovered by the DSA program, namely FRB 190523 (Ravi et al. 2019), and FRB 20220319D (Ravi et al. 2023), in our comparison sample. We then attempt to demonstrate the formulation of delay-time distribution analysis for FRB progenitors using the two FRBs reported in this article.

4.1. Comparison with the Background Galaxy Population

We use the GALEX-SDSS-WISE Legacy Catalog (GSWLC; Salim et al. 2018) for the background galaxies population with redshift ≤0.2 and PRIMUS (Moustakas et al. 2013) data set for the background galaxies population with redshift ≥0.2 but ≤0.6 to match the characteristic redshift range of FRBs. Therefore, our background galaxies population data set comprises ~77,000 galaxies with an approximately uniform distribution of galaxy redshifts. We note that there are significant systematics involved in such comparative analysis. These systematics arise from the differences in the SEDmodeling approaches, such as parameterization of the star formation histories and measurements of recent SFR. For a more accurate comparison, one must use derived galaxy properties with non-parametric star formation history SED modeling. However, due to unavailability of such a public data set, we resort to using parametric derived background galaxy properties.

The left-hand panel of Figure 5 shows the distribution of FRB hosts in the space of stellar mass and recent SFR along with the redshift evolution of the boundary between starforming and quiescent galaxies (Moustakas et al. 2013). We observe that the host of FRB 20220914A is a typical starforming galaxy. While most of the FRB hosts lie around the star-forming main sequence, the host of FRB 20220509G is exceptional as a quiescent galaxy. Recently, Gordon et al. (2023) used the mass-doubling number criterion of Tacchella et al. (2022) to classify galaxies as star-forming, transitioning, and quiescent. Since this criterion was developed on galaxy properties that were derived using non-parametric star formation histories, it is more appropriate to classify the hosts of our two FRBs using the mass-doubling number. The massdoubling number for the hosts of FRB 20220914A and FRB 20220509G are 1.823 and 0.007, thus classifying them as

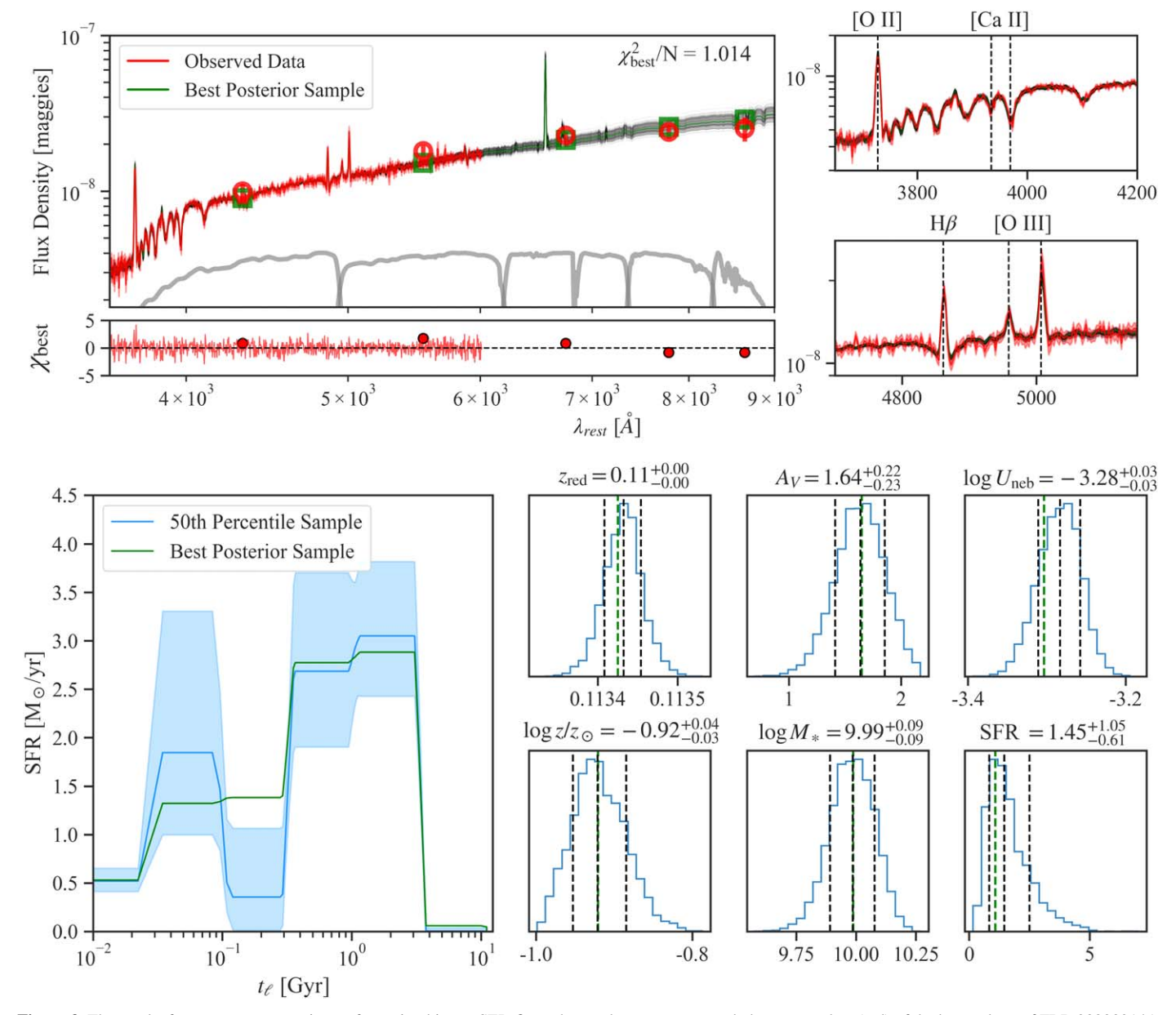


Figure 3. The results from a non-parametric star formation history SED fit to observed spectroscopy and photometry data (red) of the host galaxy of FRB 20220914A, J1848+73. The top panel shows the SED fit with residuals for the best posterior sample (green) and 100 random posterior samples (black). The plots zoomed at various absorption and emission features indicate the accuracy of our SED fits. The bottom panel displays the star formation history and constrained galaxy parameters with 16th and 84th percentiles indicated. The derived parameters for J1848+73 are consistent with a typical star-forming galaxy.

star-forming and quiescent galaxies, respectively. This is consistent with our previous arguments.

The right-hand panel of Figure 5 shows the color–magnitude diagram with the distribution of background galaxies and FRB hosts plotted. Due to the unavailability of colors and magnitudes of the 23 FRB hosts published in Gordon et al. (2023), we use the data from Bhandari et al. (2022). While most of the FRB hosts are late-type galaxies with young stellar populations and significant ongoing star formation, the host of FRB 20220509G stands out as an early-type galaxy with an old stellar population in the red cloud of the background galaxies population in the color–magnitude diagram.

We further compare the stellar mass and SFR of the host of FRB 20220509G with the typical values for elliptical and spiral galaxies, which are computed using the galaxy classifications in Galaxy Zoo data set (Lintott et al. 2011). We note that the

typical redshift range for galaxies in the Galaxy Zoo data set is \lesssim 0.2, which is consistent with the redshift of the host of FRB 20220509G. All of the queries were performed using CasJobs (OMullane et al. 2005). The stellar mass and SFRs for typical spiral galaxies are $\log M_*(M_\odot) = 10.77^{+0.39}_{-0.62}$ and $\log SFR (M_\odot \text{ yr}^{-1}) = 0.44^{+0.46}_{-0.74}$, whereas for typical elliptical galaxies they are $\log M_*(M_\odot) = 11.24^{+0.36}_{-0.56}$ and $\log SFR (M_\odot \text{ yr}^{-1}) = -0.97^{+1.11}_{-0.58}$. Both the stellar mass and SFR for the host galaxy of FRB 20220509G are consistent with elliptical galaxies, thus providing additional evidence for it being an elliptical galaxy.

4.2. Comparison with Extragalactic Transients

A comparison of the environment of transients is important to identify the possible similarities in their progenitors and formation

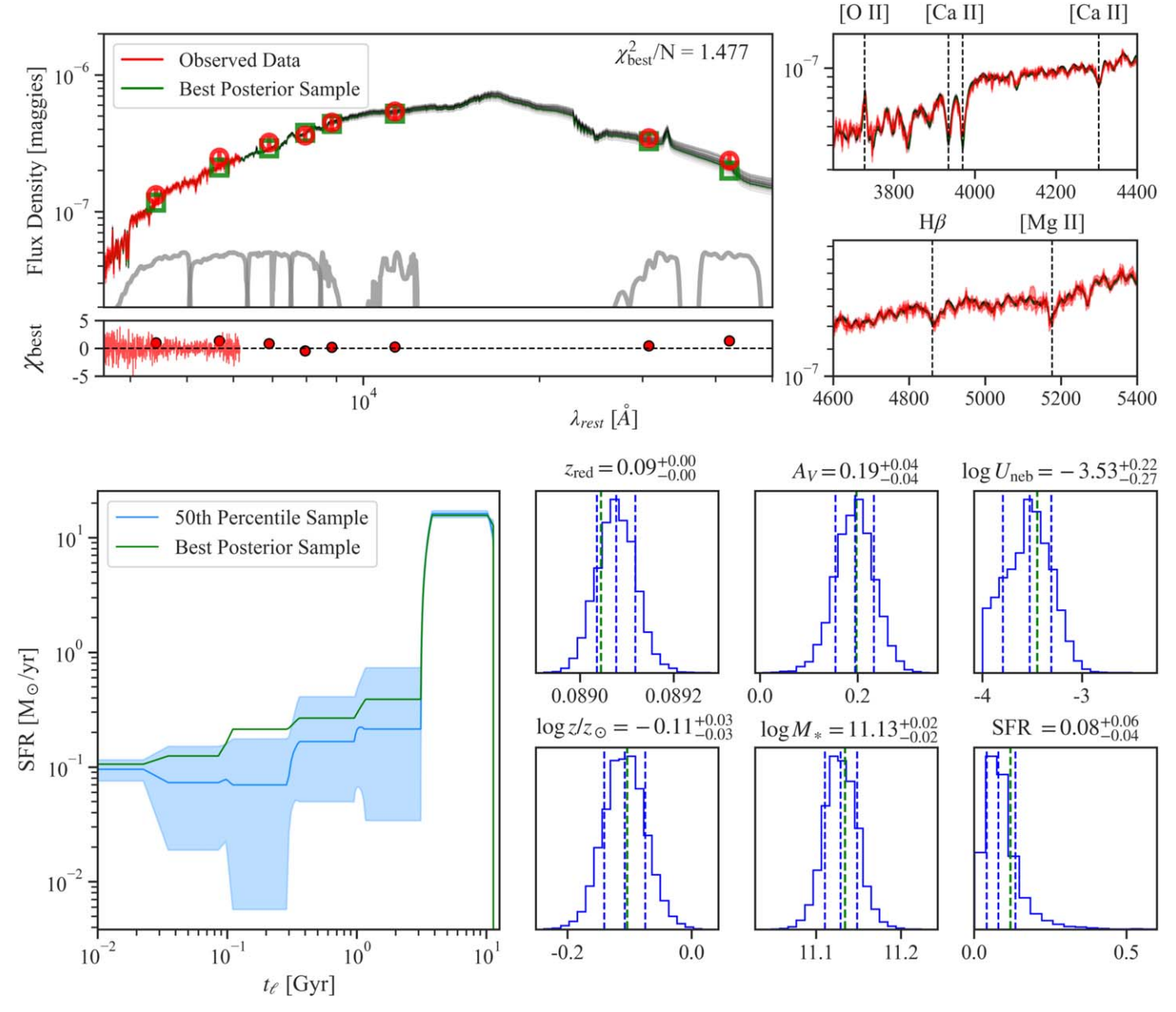


Figure 4. The results from a non-parametric star formation history SED fitted to observed spectroscopy and photometry data (red) of the host galaxy of FRB 20220509G, J1850+70. The top panel shows the SED fit with residuals for the best posterior sample, along with 100 random posterior samples (black). The zoomed version of the plots display the accuracy of our fits to various absorption and emission features. The bottom panel displays the star formation history and constrained galaxy parameters with 16th and 84th percentiles indicated. The high stellar mass and low recent SFR of J1850+70 with low dust attenuation are indicative of a massive elliptical galaxy.

channels. Several such investigations have been conducted in the past (Bhandari et al. 2020; Heintz et al. 2020; Li & Zhang 2020; Safarzadeh et al. 2020; Bochenek et al. 2021; Mannings et al. 2021; Bhandari et al. 2022). We augment these works by specifically considering our two new FRB hosts. We compare the specific SFRs (sSFRs) of the host galaxies of FRBs with Type Ia supernovae (Lampeitl et al. 2010), ultra-luminous X-ray 2020), sources (ULX; Kovlakas et al. super-luminous supernovae (SLSNe; Schulze et al. 2021; Taggart & Perley 2021), core-collapse supernovae (CCSNe; Schulze et al. 2021; Taggart & Perley 2021), short gamma-ray bursts (sGRB; Nugent et al. 2022), and long gamma-ray bursts (IGRB; Vergani et al. 2015; Taggart & Perley 2021). We note that the hosts of transients in our comparison sample have a huge variance. The redshifts of FRB hosts in our sample are $z = 0.214^{+0.125}_{-0.120}$, where quoted values are

the 16th, 50th, and 84th percentiles of the redshift distribution. Meanwhile, the redshift distribution of other transient's hosts is quite varied, including $z=0.009^{+0.018}_{-0.006}$ for ULX, $z=0.226^{+0.106}_{-0.114}$ for SLSNe, $z=0.039^{+0.047}_{-0.022}$ for CCSNe, $z=0.485^{+0.320}_{-0.262}$ for sGRB and $z=0.283^{+0.422}_{-0.194}$ for IGRB. Therefore, for a fair comparison, one must account for the redshift evolution of the galaxy star-forming main sequence. The stellar mass and SFR need to be corrected to statistically represent all of the galaxies at the present epoch. To this end, we adopt the formulation developed by Bochenek et al. (2021) to convert the stellar mass and SFRs of all of the hosts of transients to their respective values at z=0, where the p-value of stellar mass and SFR relative to the distribution of star-forming galaxies is conserved at the redshift of the galaxy and the current epoch.

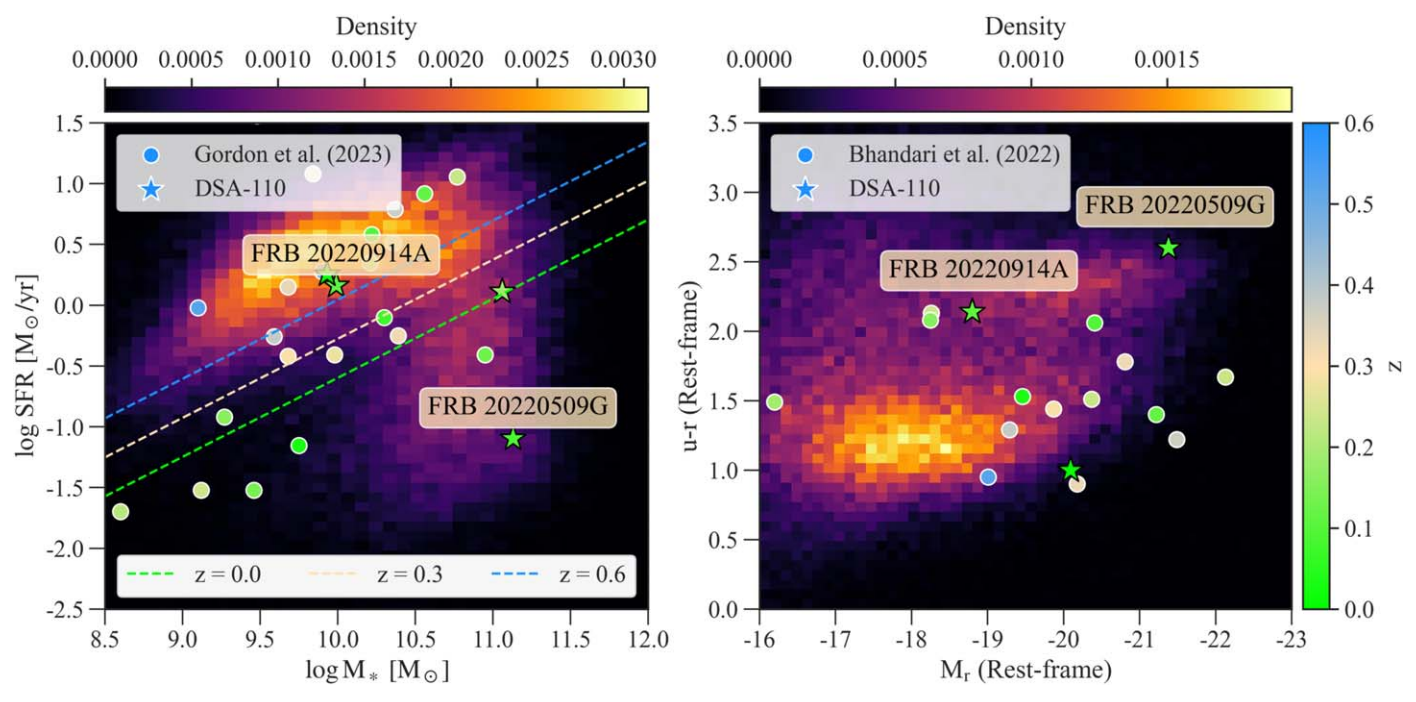


Figure 5. Comparison of the host galaxies of FRBs (including the sample published in Gordon et al. (2023)) with the background galaxies from the PRIMUS data set (Moustakas et al. 2013). The stellar mass–SFR plot in the left-hand panel with redshift evolution of the boundary between star-forming and quiescent galaxies (Moustakas et al. 2013) indicates that while the host galaxy of FRB 20220914A is a typical star-forming galaxy, the host galaxy of FRB 20220509G stands out as a quiescent galaxy in the population of known FRB hosts. The color–magnitude diagram in the right-hand panel shows that the host galaxy of FRB 20220509G is red and composed of older stellar population as compared to the rest of the FRB hosts population (Bhandari et al. 2022).

Table 2
Summary of Observed and Derived Parameters of the Host Galaxies of the Two FRBs Presented in this Article

Parameter	FRB 20220914A	FRB 20220509G 0.0894 ± 0.0001
$z_{\rm red}$	0.1139 ± 0.0001	
$D_{\rm L}^{\rm a}$ [Mpc]	534.94	412.95
d ^b [kpc]	9.87	3.80
$r_e^{\mathbf{c}}$ [kpc]	2.67	6.64
$\log M_* [M_{\odot}]$	$9.99^{+0.09}_{-0.09}$	$11.13^{+0.02}_{-0.02}$
SFR ^d	$1.45^{+1.05}_{-0.61}$	$0.08^{+0.06}_{-0.04}$
log(sSFR) [Gyr ⁻¹]	$-0.82^{+0.20}_{-0.22}$	$-3.23^{+0.23}_{-0.29}$
$\log z/z_{\odot}$	$-0.92^{+0.04}_{-0.03}$	$-0.11^{+0.03}_{-0.03}$
A_V	$1.64^{+0.22}_{-0.23}$	$0.19^{+0.04}_{-0.04}$
$U_{ m neb}$	$-3.28^{+0.03}_{-0.03}$	$-3.53^{+0.22}_{-0.27}$
u - r (Rest Frame)	$2.14^{+0.10}_{-0.11}$	$2.60^{+0.03}_{-0.02}$
g - r (Rest Frame)	$0.69^{+0.04}_{-0.04}$	$0.89^{+0.01}_{-0.01}$
M _r (Rest Frame)	$-18.80^{+0.02}_{-0.02}$	$-21.38^{+0.01}_{-0.01}$
Milky Way $E(B - V)$	-0.36	-0.06

Notes. Note that all the derived galaxy properties have been measured using the SED analysis. The quoted measurements are the 16th, 50th, and 84th percentiles.

Figure 6 shows the cumulative distributions of sSFR in the hosts of the different transient samples, together with the hosts of FRBs 20220914A and 20220509G. The sSFR of the FRB 20220914A host is consistent with essentially all transient populations. However, only sGRBs have been observed (among the samples under consideration) in galaxies with a similarly low

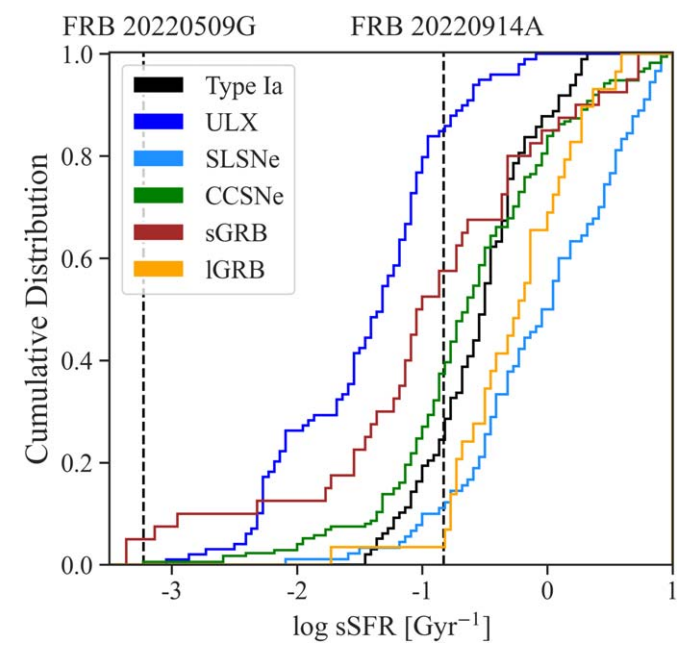


Figure 6. The cumulative distributions of sSFRs for different extragalactic transients, evaluated at redshift z=0 (see text for details). The vertical lines show the sSFRs of the new FRB hosts we present herein.

sSFR as the host of FRB 20220509G. This is consistent with a scenario wherein, like sGRBs, FRB 20220509G may have occurred long after the star formation event that formed its progenitor (e.g., Zevin et al. 2022). Ravi & Lasky (2014) also highlighted the possibility of FRB progenitor formation in binary neutron star mergers, which give rise to sGRBs. As above, similar results are obtained for stellar mass and SFR distributions.

^a Luminosity distance.

^b Projected physical offset from galaxy center.

^c Effective radius.

^d Recent SFR averaged over the last 100 Myr.

We choose not to quantitatively compare the distributions of host-galaxy properties of these transient samples and the FRB host population discussed above. Optical host selection effects, where the magnitude-limited data may lead to misidentification of the host galaxies and only brighter hosts are chosen for further analysis, affect the stellar mass and SFR distributions, which increases the median values of the respective parameters (Seebeck et al. 2021). The inconsistency in the SED-analysis approaches and recent SFR indicators that are used to derive the galaxy properties of all transients introduces systematics that are difficult to quantify. For example, Taggart & Perley (2021) use a parametric exponentially-declining star formation history model to derive present-day star formation rates for the CCSNe, SLSNe, and IGRBs included in Figure 6, whereas we use a non-parametric star formation history. A more detailed analysis that addresses some of these issues will be presented in a future work with a bigger FRB sample (Law et al. 2023, in preparation).

4.3. Delay-time Distribution

Analyses of the host galaxies of transients yield information of the underlying stellar populations, which can allow us to put novel constraints on their progenitor channels. The delay-time distribution of transients can give us insights into the birth properties of their progenitors and can help us to disentangling multiple progenitor possibilities. For example, models of single-degenerate ONe/CO white dwarf -helium star binary channel of accretion-induced collapse events, which lead to the formation of intermediate-mass binary pulsars with short orbital periods, predict short delay times (Wang & Liu 2020). Meanwhile, models of single-degenerate ONe white dwarf red giant binary channel of accretion-induced collapse events, which lead to the formation of young millisecond pulsars in globular clusters, predict longer delay times (Wang & Liu 2020). Furthermore, the delay-time distribution of transients is also a valuable probe of their formation rates. The expected local binary neutron star merger rate evolution computed using the delay-time distribution of sGRBs has been found to be consistent with constraints from gravitational wave observations (Zevin et al. 2022). This also affirms that these binary compact object mergers are the progenitors of sGRBs (Zevin et al. 2022).

Motivated by such studies, we attempt to constrain the delay-time distribution of FRBs using our two galaxy-cluster FRBs. We note that the delay-time distributions for repeating and non-repeating FRBs may be different due to possible differences in their progenitor channels. Here, we focus on computing the delay-time distribution using our two apparently non-repeating FRBs. We define the delay time, t_d , as the time between the recent starburst in the galaxy and the time an FRB occurs. Essentially, $t_d = t_* + t_{\rm age}$, where t_* is the time between the formation of progenitor stars and the formation of the FRB progenitors, and $t_{\rm age}$ is the age of the FRB source. In this initial analysis, we assume that $t_{\rm age} \ll t_*$, and hence, $t_d \approx t_*$. Following the formulation described in Zevin et al. (2022), we parameterize the delay-time distribution as a power-law distribution in the range of $t_{\rm min}$ to $t_{\rm max}$ of stellar evolution timescale with a spectral index α ,

$$p(t_d, \ \alpha, \ t_{\min}, \ t_{\max}) = \begin{cases} \mathcal{N}t_d^{\alpha}, \ t_{\min} \leqslant t_d \leqslant t_{\max}, \\ 0, \quad \text{otherwise} \end{cases}$$
(1)

where \mathcal{N} is the normalization. For a given host galaxy i and a star formation history posterior sample j, the expected rate of

FRBs \dot{n}_i^j at redshift z_i^j is defined as,

$$\dot{n}_{i}^{j} = \int_{z'=\infty}^{z'=z_{i}^{j}} p(t'_{lb} - t_{lb}|\alpha, \ t_{\min}, \ t_{\max}) \lambda \psi_{i}^{j}(z') \frac{dt}{dz}(z') dz', \ (2)$$

where $t_{\ell b}'$ and $t_{\ell b}$ are the lookback times at redshifts z' and z_i' , respectively; λ is the FRB source formation efficiency, which has been assumed to be $10^{-5}\,M_\odot^{-1}$; $\psi_i^j(z')$ is the non-parametric star formation history derived using Prospector; and dt/dz is defined using the standard cosmological model. Assuming that the probability of occurrence of an FRB follows a Poisson distribution, the hyperlikelihood of observing the FRB from the particular galaxy can be written as,

$$\mathcal{L}(\psi_i|\alpha, t_{\min}, t_{\max}) \approx \frac{\mathcal{A}}{N} \sum_{i=1}^{N} (\dot{n}_i^j \Delta t) e^{-\dot{n}_i^j \Delta t},$$
 (3)

where Δt is a fiducial observing time of 10 yr and \mathcal{A} is the normalization. Assuming that our observations of FRB 20220914A and FRB 20220509G are independent, the hyperposterior is,

$$P(\alpha, t_{\min}, t_{\max}|obs) \propto \prod_{i=1}^{2} \mathcal{L}(\psi_{i}|\alpha, t_{\min}, t_{\max}) \times \pi,$$
 (4)

where $\pi(\alpha, t_{\min}, t_{\max})$ is the prior on the delay-time distribution parameters, which are uniform in the range [-3, 1], [1 Myr, 2 Gyr] and [2 Gyr, 13.7 Gyr], respectively. We choose the prior range for α based on the typical observationally-constrained values for other transients, such as CCSNe (Zapartas et al. 2017), Type Ia Supernovae (Maoz & Graur 2017), and sGRBs (Zevin et al. 2022). An independent (of other transients) choice of delay-time distribution power-law index requires more constraints from a theoretical understanding of their progenitors. The prior ranges of t_{\min} and t_{\max} are based on the observed star formation histories of FRB host galaxies. As observed in this work and by Gordon et al. (2023), FRBs have been found in both late-type and early-type galaxies, with various types of star formation histories, i.e., rising, delayed- τ exponentially-declining, τ -linear exponentially-declining, poststarburst, and rejuvenating. Hence, to allow for flexibility, we choose to use wide priors on t_{min} and t_{max} . Future work with bigger host samples should allow for more informed priors on these three parameters. We use precomputed grids of likelihoods and interpolate when evaluating the likelihood function. We use the dynesty nested sampler (Speagle 2020) in the framework of Bilby (Ashton et al. 2019) for generating posterior distributions.

Our constraints on the delay-time distribution parameters are shown in Figure 7. Given the small sample size, we cannot make meaningful statements regarding the posteriors of the three delay-time distribution parameters. Nevertheless, it is evident that these three parameters are not correlated. The multiple peaks in the posterior distribution of $t_{\rm min}$ indicate the importance of non-parametric star formation histories in constraining the delay-time distribution parameters because all possible starbursts are taken into account, which would otherwise be missed in a parametric star formation history. Future studies with a bigger hosts sample may help to constrain these parameters better and shed some light on the evolutionary histories of FRB sources and the FRB rate evolution with redshift.

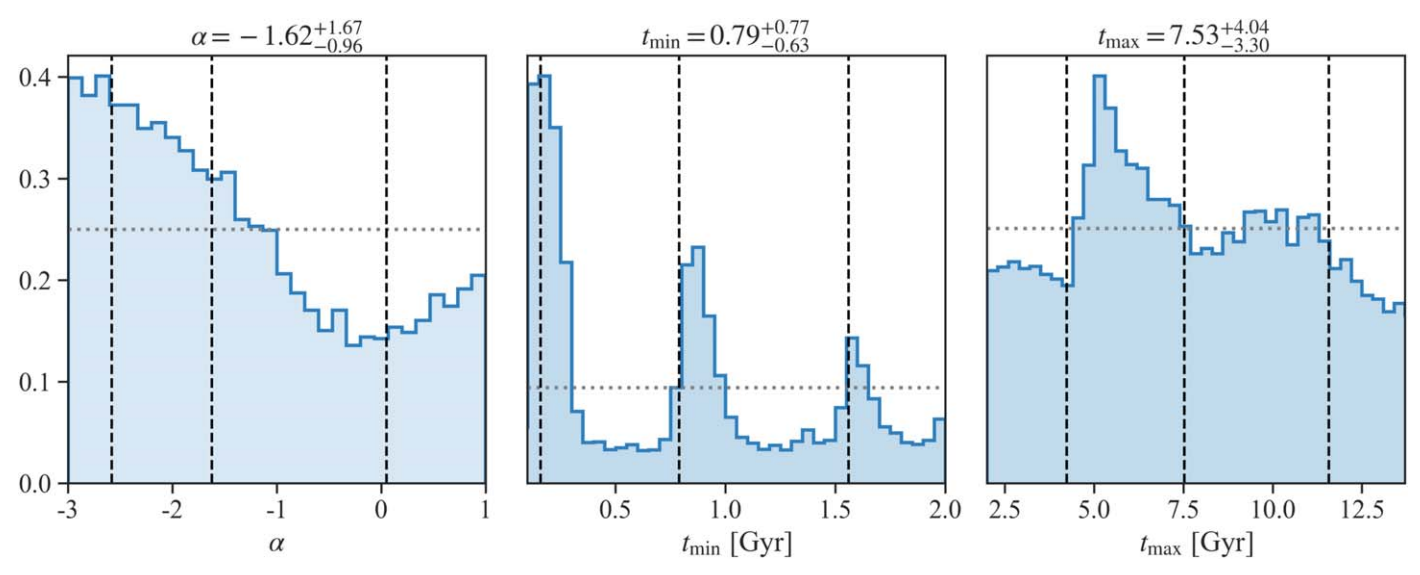


Figure 7. The kernel density estimates of the posteriors of the delay-time distribution parameters for FRBs constrained using non-parametric star formation histories of the host galaxies of FRB 20220914A and FRB 20220509G. The gray dotted line depicts our priors on these parameters and the vertical lines show the 16%, 50%, and 84% credible regions. The multi-peaked feature in the t_{\min} posterior distribution is a characteristic feature that is embedded from non-parametric star formation histories.

Comparing our constraints with the delay-time distribution of other transients, we note the similarity in the power-law index of $\alpha = -1.65^{+0.39}_{-0.38}$ with sGRBs (Zevin et al. 2022). Furthermore, a long tail in the delay-time distribution adds to the evidence that FRBs can be produced by the old stellar population (O'Connor et al. 2022), similar to sGRBs with a $t_{\rm min}$ > 88 Myr and $t_{\rm max}$ > 7.95 Gyr (Zevin et al. 2022). The delay times for CCSNe from the death of single massive stars is typically less than ~ 100 Myr (Zapartas et al. 2017). However, our delay-time distribution and star formation histories indicate that FRB progenitors have delay times greater than ~ 100 Myr. These delay times fall into the regime of the second formation channel of CCSNe, where a massive star in an interacting binary system collapses under its own gravity, which extends their delay times up to 250 Myr (Zapartas et al. 2017). There are evident dissimilarities in the delay-time distribution of Type Ia SNe and FRBs, including their delay-time range, where the maximum Type Ia SNe rate is at the current epoch (Maoz & Graur 2017). To further disentangle FRB progenitors from the relatively well-understood transients, we look forward to constraining the delay-time distribution with bigger host galaxies samples in the coming years.

5. Summary and Discussion

FRBs have been found in a wide variety of environments (Petroff et al. 2022), including star-forming regions in dwarf galaxies (Bassa et al. 2017; Bhandari et al. 2023), spiral galaxies (Marcote et al. 2020; Fong et al. 2021; Mannings et al. 2021), at significant offsets from star-forming regions (Tendulkar et al. 2021), and globular clusters (Bhardwaj et al. 2021; Kirsten et al. 2022). However, none have been previously associated with galaxy clusters. This and our companion paper, Connor et al. (2023), report the discovery of two FRBs in massive galaxy clusters. The host galaxy of FRB 20220914A resides in the galaxy-cluster A2311 (Abell 1958) with $M_{180} = 2.4 \times 10^{14} M_{\odot}$ as per the DESI Legacy Imaging Surveys Data Release 9 (DR9) group/cluster catalog (Dey et al. 2019) and the host galaxy of FRB

20220509G resides in the galaxy-cluster A2310 (Abell 1958) with $M_{180} = 2.5 \times 10^{14} M_{\odot}$. The relative redshifts of the host galaxies and the brightest cluster galaxy (BCG) are within 0.001, which implies a recession velocity of roughly 400 km s⁻¹. This small difference in the recession velocity between the cluster BCG and these galaxies suggests that these galaxies are likely to be bound. As discussed in Connor et al. (2023), these galaxies are not in the front of the cluster because of the large excess DM, which agrees with the expected ICM contribution, and this excess DM cannot be explained by the host galaxy. Furthermore, the host galaxies cannot be significantly behind the cluster because of an over-density argument presented in Connor et al. (2023). So, while we cannot know the exact radial position within the cluster, its DM suggests that it is roughly halfway through the ICM along the line of sight. Out of the 21 non-repeating FRBs that we consider as a sample (see Section 4), only ~9.5% of the FRBs are found in galaxy-cluster environments. This is broadly consistent with the value of $\sim 10\%$ for the overall fraction of stellar mass in galaxy clusters (Fukugita et al. 1998). However, this result may be surprising if the occurrence of FRBs is driven by ongoing star formation because galaxy clusters contribute negligibly to the present-day cosmic star formation rate density (e.g., Chiang et al. 2017).

The SFR of galaxies is very well known to be correlated with the galaxy number density (Kauffmann et al. 2004). The galaxies at the core of the galaxy clusters have lower SFRs as compared to the infalling galaxies (Barsanti et al. 2018). We use the stellar mass–SFR relations from Paccagnella et al. (2016) to compare the SFR in our host galaxies with typical galaxies in clusters. We note that the relations used for these comparisons of cluster-centric distances are based on radial "projected distance," R, and the radius at which the average enclosed density is 200 times the critical density, R_{200} . These are $R = 520 \pm 50$ kpc, $R_{200} = 1134$ kpc for the host galaxy of FRB 20220914A and $R = 870 \pm 50$ kpc, $R_{200} = 1120$ kpc for the host galaxy of FRB 20220509G, as reported in Connor et al. (2023). We note that we used a conversion factor of 1.4 to convert R_{500} reported in Connor et al. (2023) to R_{200} . Based on

these calculations, the cluster-centric distances for the host of FRB 20220914A and FRB 20220509G are $R/R_{200} \sim 0.46$ and $R/R_{200} \sim 0.78$, respectively. While the low recent SFR of the host galaxy of FRB 20220509G in a galaxy cluster at the respective cluster-centric distance is not unusual, the recent SFR of the host galaxy of FRB 20220914A, which is a typical star-forming galaxy, is marginally higher than the typical SFR of galaxies in clusters at a cluster-centric distance of R/R_{200} \sim 0.46 (Paccagnella et al. 2016). Given that the galaxy clusters are extremely effective at cutting off star formation in galaxies by stripping off the cold gas needed for stellar birth, significant star formation in a galaxy close to the core of the cluster is unusual. Meanwhile, the host galaxy of FRB 20220509G is a red, old, massive elliptical galaxy, with low SFR, which is typical of quenched galaxies found in galaxy clusters (Laganá & Ulmer 2018). Notably, this is the first example of a likely massive elliptical FRB host galaxy.

The discovery of FRBs in the spiral arms of late-type galaxies and galaxies with higher sSFR supports the view that FRBs should have short delay times. Although most of the FRBs found to date are associated with star-forming galaxies, the quiescent and elliptical host of FRB 20220509G adds diversity to the known FRBs host galaxy population. The origin of FRBs in quiescent elliptical galaxies and globular clusters adds to the evidence that some FRB progenitors have longer delay times. Together, these environments are inconsistent with a single population, thus hinting toward a broad delay-time distribution and suggesting multiple formation channels for FRBs. The origin of FRB 20220509G in an old stellar population disfavors the possibility of formation by young highly magnetized magnetars in a core-collapse supernova. This is further supported by the fact that only 0.3% of the core-collapse supernovae occur in elliptical galaxies (Irani et al. 2022).

The old stellar population in elliptical galaxies supports multiple possibilities about the progenitor of FRB 20220509G. The likelihood of the formation of binary neutron stars in old elliptical galaxies with negligible ongoing star formation opens up the possibility of an FRB source that was formed via binary neutron star merger (Eichler et al. 1989; Narayan et al. 1992; Belczynski et al. 2018; Perna et al. 2022). Second, this particular host environment also supports progenitor formation channels in globular cluster environments due to their higher number density in elliptical galaxies (Lim et al. 2020). The high mass of the host galaxy could also favor an accretion-induced collapse of a white dwarf to a neutron star (Ravi et al. 2019). The remnant white dwarf that is formed in a typical binary white dwarf merger has long been known as a probable progenitor of Type Ia supernovae, where 99% of Type Ia supernovae in elliptical galaxies likely occur via this formation channel (Lipunov et al. 2011). If one of the merging white dwarfs has a significant magnetic field, then the merger may result in the formation of a magnetar, which can then power an FRB (King et al. 2001; Kashiyama et al. 2013; Kundu & Ferrario 2020). Similar formation channels were also proposed by Kirsten et al. (2022) upon the association of FRB 20200120E with a globular cluster in M81, due to the high probability of formation of binaries with short orbital periods in globular clusters (Tauris et al. 2013; Wang & Liu 2020). The horizon of research in modeling the progenitors of FRBs must be broadened to incorporate such formation channels of these exotic transients.

Acknowledgments

The authors thank the staff members of the Owens Valley Radio Observatory and the Caltech radio group, including Kristen Bernasconi, Stephanie Cha-Ramos, Sarah Harnach, Tom Klinefelter, Lori McGraw, Corey Posner, Andres Rizo, Michael Virgin, Scott White, and Thomas Zentmyer. Their tireless efforts were instrumental to the success of the DSA-110. The DSA-110 is supported by the National Science Foundation Mid-Scale Innovations Program in Astronomical Sciences (MSIP) under grant AST-1836018. We acknowledge the use of the VLA calibrator manual and the radio fundamental catalog. Some of the data presented herein were obtained at the W. M. Keck Observatory, which is operated as a scientific partnership among the California Institute of Technology, the University of California, and the National Aeronautics and Space Administration. The Observatory was made possible by the generous financial support of the W. M. Keck Foundation.

This research uses services or data provided by the Astro Data Lab at NSFs NOIRLab. NOIRLab is operated by the Association of Universities for Research in Astronomy (AURA), Inc., under a cooperative agreement with the National Science Foundation. This research has made use of the NASA/IPAC Extragalactic Database (NED), which is operated by the Jet Propulsion Laboratory, California Institute of Technology, under contract with the National Aeronautics and Space Administration. This research has made use of NASAs Astrophysics Data System Bibliographic Services. This research has made use of the VizieR catalog access tool, CDS, Strasbourg, France (DOI:10.26093/cds/vizier). The original description of the VizieR service was published in 2000, A&AS 143, 23. This research made use of Astropy, a community-developed core Python package for Astronomy.

Facilities: DSA-110, Keck:I (LRIS) (Oke et al. 1995).

Software: astropy (Astropy Collaboration 2013, 2018), NumPy (Harris et al. 2020), SciPy (Virtanen et al. 2020), Matplotlib (Hunter 2007), lpipe (Perley 2019), pPXF (Cappellari 2017, 2022), Prospector (Johnson et al. 2021), emcee (Foreman-Mackey et al. 2013), astropath (Aggarwal et al. 2021), astro-datalab.

Appendix A SED Analysis Methodology

A.1. Treating Nebular Emission

Modeling nebular emission in spectroscopic data can be tricky when fitting for photometry and spectroscopy together in Prospector. In this appendix, we outline two approaches for tackling this. For the purpose of demonstrations, we simulate an SNR = 100 SED with parametric star formation history. We chose to use an exponentially-declining star formation history parameterized by star formation timescale, $\tau = 1.25$ and age of the galaxy, $t_{\rm age} = 0.6 \times t_{\rm univ}$, where $t_{\rm univ}$ is the age of the galaxy at a redshift of $z_{\rm red} = 0.1$. The simulated photometry and spectrum represent a galaxy with a stellar mass $M_* = 10^{10} \, M_{\odot}$, metallicity $\log z/z_{\odot} = -0.2$, dust attenuation $A_V = 0.5$ and nebular ionization parameter $U_{\rm neb} = -3$. The true value of recent SFR averaged over the last 100 Myr is $\sim 0.13 \, M_{\odot}$ yr⁻¹.

To deal with nebular emission, we demonstrate two possible approaches. First, adding nebular continuum and emission lines to the model along with marginalization over the amplitude of the emission lines to account for nebular emission from

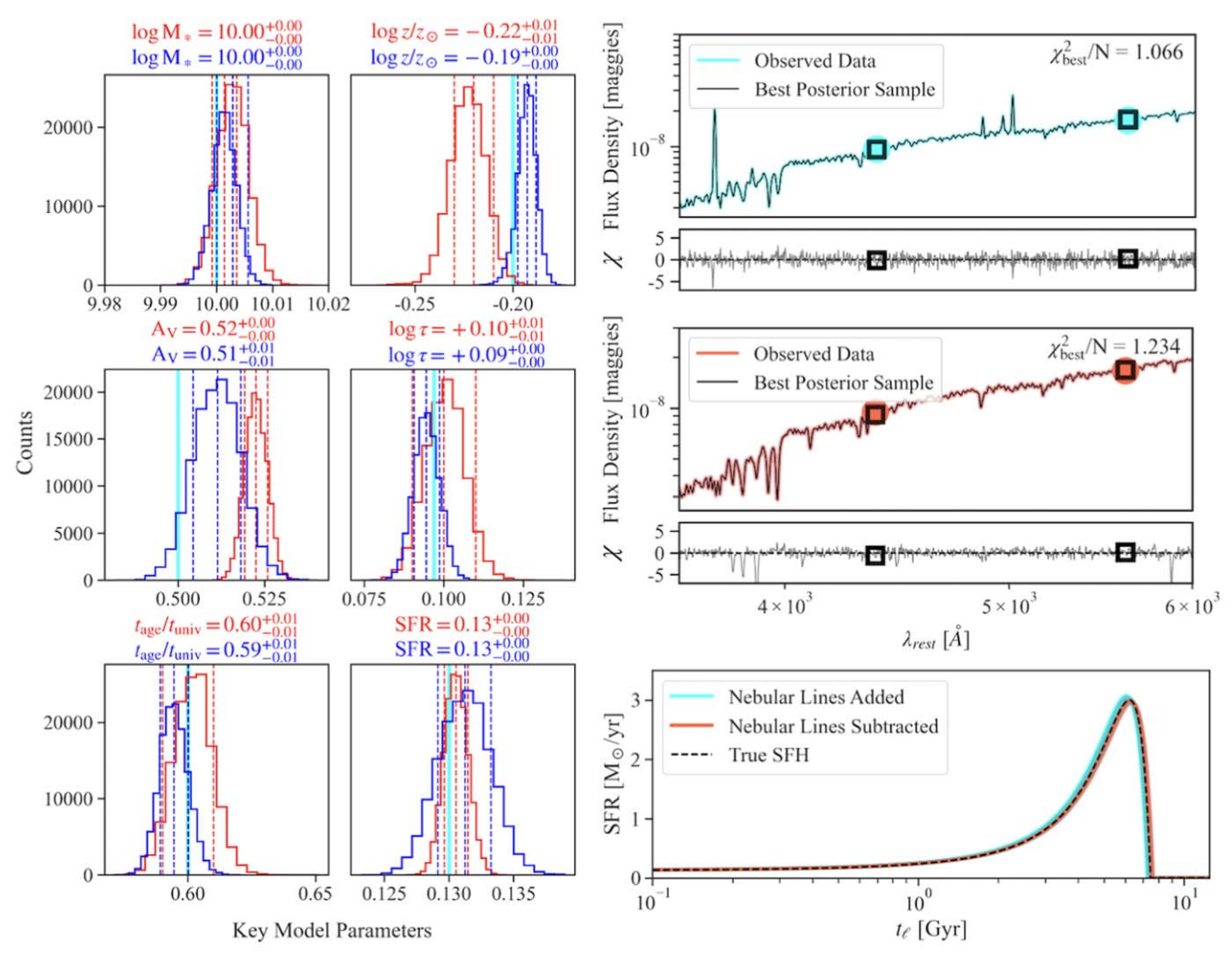


Figure 8. Comparison of different treatments for nebular emission in a galaxy. The left-hand panel shows all the simulated true values (cyan), recovered values with nebular emission lines (blue), and recovered values with nebular emission lines removed (red). We observe that the constraints are better with emission lines but both techniques yield broadly consistent values with the true values. The top (middle) right-hand panel shows the simulated spectrum with (without) emission lines and recovered best posterior sample, along with the corresponding residuals. The bottom right-hand panel shows the true and recovered star formation histories for both cases, which are consistent.

mechanisms other than star formation and nebular emission from old stellar population, as is also discussed in Johnson et al. (2021). The second approach involves subtracting the emission lines from the spectrum using the best fit for the gas component from pPXF, and then fitting the subtracted spectrum and photometry of these emission lines in Prospector with nebular continuum added to the model.

The resulting recovered star formation histories from our two experiments are shown in Figure 8. The reduced- χ^2 of the best posterior sample when including the nebular emission lines is relatively lower than the best posterior sample when removing the nebular emission lines. We observe higher χ values at the higher energy hydrogen absorption features because they are not included in the pPXF fit to the gas component. The recovered galaxy parameters are broadly consistent with the true parameters with slight deviations in metallicity and dust attenuation from their respective true values. The parameters are better constrained when nebular emission lines are included in the data. Nevertheless, both techniques are equally good at recovering the true star formation history and one may opt for either of these methods when modeling their respective galaxies.

A.2. Constraining Star Formation History

The star formation history carries the information of the times of stellar birth in a galaxy and constraining it is important to achieve meaningful constraints on the delay-time distribution. The nebular emission and absorption features in a spectrum carry detailed information about the stellar age. In this appendix, we demonstrate how accurately one can recover the star formation history with and without using the spectrum in SED fits in the presence or absence of nebular emission. For the purpose of these demonstrations, we use the same galaxy parameters as used in Appendix A.1 and the same model as described in Section 3.2 (except for changing the nebular emission based on the case under consideration).

The left-hand panel of Figure 9 displays our results when nebular emission is completely excluded from our simulations. We observe that the recovered stellar mass, metallicity, and dust attenuation are broadly consistent with the true values both when we fit for photometry alone and when we fit simultaneously for photometry and spectroscopy. However, in the absence of the spectrum, the age of the galaxy and the star formation timescale are poorly constrained, as can also be

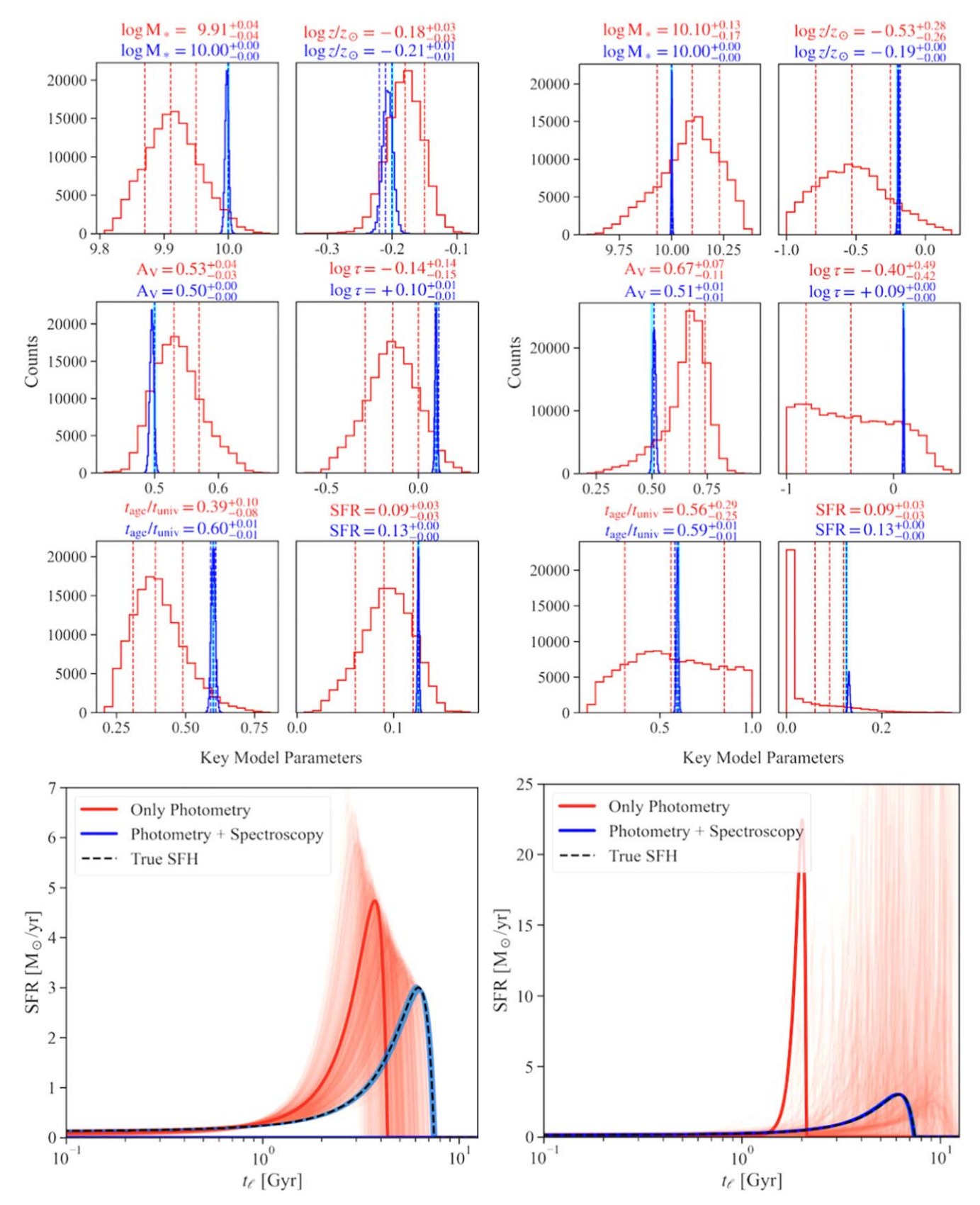


Figure 9. Demonstration of the constraints on star formation histories when fitting SED to photometry alone (red) and jointly fitting photometry and spectroscopy (blue). The injected parameters are marked in cyan. The left-hand panel shows the results when nebular emission is omitted in the model for simplification. We observe that the star formation history constrained without the spectrum is poor. Meanwhile, the addition of the nebular emission to the model makes the problem complex, leading to even poorer constraints without the spectrum, as can be seen in the right-hand panel. Hence, if accurately constraining star formation history is important for a specific science case, we recommend jointly fitting for photometry and high SNR spectrum in SED analysis.

seen in the star formation history samples plotted in the bottom left-hand panel of Figure 9. As was also noted in Johnson et al. (2021), we also observed the dust-age-metallicity degeneracy and stellar age-stellar age timescale degeneracy in our recovered parameters in the absence of the spectrum.

We further test this result by adding the nebular emission to the model. We observe that the constraints of all of the parameters are poor when compared to the case with spectrum added to the SED fits. The stellar age and stellar evolution timescale parameters essentially recover the prior. This is also evident in the corresponding recovered star formation histories with and without spectrum in the bottom panel of Figure 9. Based on these demonstrations, we strongly recommend using the spectrum to constrain the star formation histories when possible, especially when doing delay-time distribution studies.

ORCID iDs

```
Kritti Sharma  https://orcid.org/0000-0002-4477-3625
Jean Somalwar  https://orcid.org/0000-0001-8426-5732
Casey Law  https://orcid.org/0000-0002-4119-9963
Vikram Ravi  https://orcid.org/0000-0002-7252-5485
Ge Chen  https://orcid.org/0000-0003-2867-4544
Liam Connor  https://orcid.org/0000-0002-7587-6352
Jakob T. Faber  https://orcid.org/0000-0001-9855-5781
Gregg Hallinan  https://orcid.org/0000-0002-7083-4049
James W. Lamb  https://orcid.org/0000-0002-5959-1285
Myles B. Sherman  https://orcid.org/0000-0002-6573-7316
Jun Shi  https://orcid.org/0000-0002-8873-8784
Reynier Squillace  https://orcid.org/0000-0001-6748-5290
Nitika Yadlapalli  https://orcid.org/0000-0003-3255-4617
```

References

```
Abell, G. O. 1958, ApJS, 3, 211
Aggarwal, K., Budavári, T., Deller, A. T., et al. 2021, ApJ, 911, 95
Ashton, G., Hübner, M., Lasky, P. D., et al. 2019, ApJS, 241, 27
Astropy Collaboration, Price-Whelan, A. M., Sipőcz, B. M., et al. 2018, AJ,
   156, 123
Astropy Collaboration, Robitaille, T. P., & Tollerud, E. J. 2013, A&A,
  558. A33
Barsanti, S., Owers, M. S., Brough, S., et al. 2018, ApJ, 857, 71
Bassa, C. G., Tendulkar, S. P., Adams, E. A. K., et al. 2017, ApJL, 843, L8
Belczynski, K., Askar, A., Arca-Sedda, M., et al. 2018, A&A, 615, A91
Berger, E. 2009, ApJ, 690, 231
Bhandari, S., Gordon, A. C., Scott, D. R., et al. 2023, ApJ, 948, 67
Bhandari, S., Heintz, K. E., Aggarwal, K., et al. 2022, AJ, 163, 69
Bhandari, S., Sadler, E. M., Prochaska, J. X., et al. 2020, ApJL, 895, L37
Bhardwaj, M., Gaensler, B. M., Kaspi, V. M., et al. 2021, ApJL, 910, L18
Blanchard, P. K., Berger, E., & Fong, W.-f. 2016, ApJ, 817, 144
Bloom, J. S., Kulkarni, S. R., & Djorgovski, S. G. 2002, AJ, 123, 1111
Bochenek, C. D., Ravi, V., & Dong, D. 2021, ApJL, 907, L31
Bradley, L., Sipőcz, B., Robitaille, T., et al. 2022, astropy/photutils v1.5.0,
  Zenodo, doi:10.5281/zenodo.6825092
Cappellari, M. 2017, MNRAS, 466, 798
Cappellari, M. 2022, arXiv:2208.14974
Chambers, K. C., Magnier, E. A., Metcalfe, N., et al. 2016, arXiv:1612.05560
Chatterjee, S., Law, C. J., Wharton, R. S., et al. 2017, Natur, 541, 58
Chiang, Y.-K., Overzier, R. A., Gebhardt, K., & Henriques, B. 2017, ApJL,
Connor, L., Ravi, V., Catha, M., et al. 2023, ApJL, 949, L26
Conroy, C. 2013, ARA&A, 51, 393
Conroy, C., & Gunn, J. E. 2010, FSPS: Flexible Stellar Population Synthesis,
   Astrophysics Source Code Library, ascl:1010.043
Conroy, C., Gunn, J. E., & White, M. 2009, ApJ, 699, 486
Cutri, R. M., Wright, E. L., Conrow, T., et al. 2021, yCat, 2328, 0
Dey, A., Schlegel, D. J., Lang, D., et al. 2019, AJ, 157, 168
Draine, B. T., & Li, A. 2007, ApJ, 657, 810
```

```
Eichler, D., Livio, M., Piran, T., & Schramm, D. N. 1989, Natur, 340, 126
Ferland, G. J., Porter, R. L., van Hoof, P. A. M., et al. 2013, RMxAA, 49, 137
Fitzpatrick, E. L. 1999, PASP, 111, 63
Fong, W., & Berger, E. 2013, ApJ, 776, 18
Fong, W.-f., Dong, Y., Leja, J., et al. 2021, ApJL, 919, L23
Fong, W.-f., Nugent, A. E., Dong, Y., et al. 2022, ApJ, 940, 56
Foreman-Mackey, D., Hogg, D. W., Lang, D., & Goodman, J. 2013, PASP,
Fukugita, M., Hogan, C. J., & Peebles, P. J. E. 1998, ApJ, 503, 518
Gordon, A. C., Fong, W.-f., Kilpatrick, C. D., et al. 2023, arXiv:2302.05465
Green, G. 2018, JOSS, 3, 695
Hakobyan, A. A., Barkhudaryan, L. V., Karapetyan, A. G., et al. 2020,
          S, 499, 1424
Harris, C. R., Millman, K. J., van der Walt, S. J., et al. 2020, Natur, 585, 357
Heintz, K. E., Prochaska, J. X., Simha, S., et al. 2020, ApJ, 903, 152
Helou, G., Madore, B. F., Schmitz, M., et al. 1991, in Databases and On-line
  Data in Astronomy, ed. M. A. Albrecht & D. Egret (Pasadena, CA:
  IPAC), 89
Hunter, J. D. 2007, CSE, 9, 90
Irani, I., Prentice, S. J., Schulze, S., et al. 2022, ApJ, 927, 10
Johnson, B. D., Leja, J., Conroy, C., & Speagle, J. S. 2021, ApJS, 254, 22
Kashiyama, K., Ioka, K., & Mészáros, P. 2013, ApJL, 776, L39
Kauffmann, G., White, S. D. M., Heckman, T. M., et al. 2004, MNRAS,
  353, 713
Kelly, P. L., Filippenko, A. V., Modjaz, M., & Kocevski, D. 2014, ApJ,
  789, 23
Kennicutt, R. C. J. 1998, ARA&A, 36, 189
Kewley, L. J., Geller, M. J., & Jansen, R. A. 2004, AJ, 127, 2002
King, A. R., Pringle, J. E., & Wickramasinghe, D. T. 2001, MNRAS, 320, L45
Kirsten, F., Marcote, B., Nimmo, K., et al. 2022, Natur, 602, 585
Kovlakas, K., Zezas, A., Andrews, J. J., et al. 2020, MNRAS, 498, 4790
Kroupa, P. 2001, MNRAS, 322, 231
Kulkarni, S. R., Ofek, E. O., & Neill, J. D. 2015, arXiv:1511.09137
Kundu, E., & Ferrario, L. 2020, MNRAS, 492, 3753
Laganá, T. F., & Ulmer, M. P. 2018, MNRAS, 475, 523
Lampeitl, H., Smith, M., Nichol, R. C., et al. 2010, ApJ, 722, 566
Leja, J., Johnson, B. D., Conroy, C., van Dokkum, P. G., & Byler, N. 2017,
   ApJ, 837, 170
Levesque, E. M., Berger, E., Kewley, L. J., & Bagley, M. M. 2010, AJ,
  139, 694
Li, Y., & Zhang, B. 2020, ApJL, 899, L6
Lim, J., Wong, E., Ohyama, Y., Broadhurst, T., & Medezinski, E. 2020, NatAs,
Lintott, C., Schawinski, K., Bamford, S., et al. 2011, MNRAS, 410, 166
Lipunov, V. M., Panchenko, I. E., & Pruzhinskaya, M. V. 2011, NewA,
  16, 250
Mannings, A. G., Fong, W.-f., Simha, S., et al. 2021, ApJ, 917, 75
Maoz, D., & Graur, O. 2017, ApJ, 848, 25
Marcote, B., Nimmo, K., Hessels, J. W. T., et al. 2020, Natur, 577, 190
Moustakas, J., Coil, A. L., Aird, J., et al. 2013, ApJ, 767, 50
Narayan, R., Paczynski, B., & Piran, T. 1992, ApJL, 395, L83
Nugent, A. E., Fong, W.-F., Dong, Y., et al. 2022, ApJ, 940, 57
O'Connor, B., Troja, E., Dichiara, S., et al. 2022, MNRAS, 515, 4890
Oke, J. B., Cohen, J. G., Carr, M., et al. 1995, PASP, 107, 375
OMullane, W., Li, N., Nieto-Santisteban, M., et al. 2005, arXiv:0502072
Paccagnella, A., Vulcani, B., Poggianti, B. M., et al. 2016, ApJL, 816, L25
Pan, Y. C., Sullivan, M., Maguire, K., et al. 2014, MNRAS, 438, 1391
Perley, D. A. 2019, PASP, 131, 084503
Perley, D. A., Niino, Y., Tanvir, N. R., Vergani, S. D., & Fynbo, J. P. U. 2016,
     SRv, 202, 111
Perna, R., Artale, M. C., Wang, Y.-H., et al. 2022, MNRAS, 512, 2654
Petroff, E., Hessels, J. W. T., & Lorimer, D. R. 2019, A&ARv, 27, 4
Petroff, E., Hessels, J. W. T., & Lorimer, D. R. 2022, A&ARv, 30, 2
Piro, L., Bruni, G., Troja, E., et al. 2021, A&A, 656, L15
Planck Collaboration, Ade, P. A. R., Aghanim, N., et al. 2014, A&A, 571, A16
Ravi, V., Catha, M., Chen, G., et al. 2023, arXiv:2301.01000
Ravi, V., Catha, M., D'Addario, L., et al. 2019, Natur, 572, 352
Ravi, V., & Lasky, P. D. 2014, MNRAS, 441, 2433
Rodríguez, S., & Padilla, N. D. 2013, MNRAS, 434, 2153
Safarzadeh, M., Prochaska, J. X., Heintz, K. E., & Fong, W.-f. 2020, ApJL,
Salim, S., Boquien, M., & Lee, J. C. 2018, ApJ, 859, 11
Sánchez-Blázquez, P., Peletier, R. F., Jiménez-Vicente, J., et al. 2006,
   MNRAS, 371, 703
Schulze, S., Yaron, O., Sollerman, J., et al. 2021, ApJS, 255, 29
Seebeck, J., Ravi, V., Connor, L., et al. 2021, arXiv:2112.07639
```

Skrutskie, M. F., Cutri, R. M., Stiening, R., et al. 2006, AJ, 131, 1163 Speagle, J. S. 2020, MNRAS, 493, 3132 Svensson, K. M., Levan, A. J., Tanvir, N. R., Fruchter, A. S., & Strolger, L. G.

2010, MNRAS, 405, 57
Tacchella, S., Conroy, C., Faber, S. M., et al. 2022, ApJ, 926, 134
Taggart, K., & Perley, D. A. 2021, MNRAS, 503, 3931
Tauris, T. M., Sanyal, D., Yoon, S. C., & Langer, N. 2013, A&A, 558, A39
Tendulkar, S. P., Bassa, C. G., Cordes, J. M., et al. 2017, ApJL, 834, L7

Tendulkar, S. P., Gil de Paz, A., Kirichenko, A. Y., et al. 2021, ApJL, 908, L12
Vergani, S. D., Salvaterra, R., Japelj, J., et al. 2015, A&A, 581, A102
Virtanen, P., Gommers, R., Oliphant, T. E., et al. 2020, NatMe, 17, 261

Wang, B., & Liu, D. 2020, RAA, 20, 135 Yan, R., Newman, J. A., Faber, S. M., et al. 2006, ApJ, 648, 281 Zapartas, E., de Mink, S. E., Izzard, R. G., et al. 2017, A&A, 601, A29

Zevin, M., Nugent, A. E., Adhikari, S., et al. 2022, ApJL, 940, L18